Supplementary Information

Mid-infrared light resonance-enhanced proton conductivity in ceramics

Haobo Li[1], Yicheng Zhu[1], Zihan Zhao[1], Ruixin Ma[1], Wenjie Wan[1,2,], and Qianli Chen[1,*]*

1 University of Michigan – Shanghai Jiao Tong University Joint Institute, Shanghai Jiao Tong University, Shanghai 200240, China

2 Department of Physics and Astronomy, Shanghai Jiao Tong University, Shanghai 200240, China

Corresponding authors

Qianli Chen – orcid.org/0000-0001-8460-0596; Email: qianli.chen@sjtu.edu.cn

Wenjie Wan – orcid.org/0000-0002-9743-3480; Email: wenjie.wan@sjtu.edu.cn

Additional characterization

X-ray diffraction (XRD) patterns of protonated and dry $BaZr_{0.8}Y_{0.2}O_{3-\delta}$ (BZY) powder were measured by an X-ray diffractometer (Rigaku Mini Flex 600, Cu Kα, λ = 1.5405 Å). The lattice constants (*a*) for the protonated and dry samples are 4.232 Å and 4.214 Å, respectively, indicating the chemical expansion of lattice due to proton incorporation. O–O separation of protonated BZY was calculated as 2.992 Å by taking $a/\sqrt{(2)}$ for the protonated samples.[1]

SEM images of sintered BZY pellets were characterized by a field emission scanning electron microscope (ThermoFisher Apreo 2 SEM, acceleration voltage 15 kV, magnification 1−2.5 kX). Thermogravimetric analysis (TGA) and differential scanning calorimetry (DSC) were performed on protonated BZY in dry N_2 from room temperature to 900 °C with a heating rate of 10 °C/min characterized by a simultaneous thermal analyser (STA) (Netzsch STA 449 F3 Jupiter). The proton concentration of protonated BZY was measured by a Karl-Fischer moisture titrator (KEM MKC-710S) in dry N_2 at 900 °C. The Karl-Fischer titration and calculation of proton concentration were conducted following previous work by Han et al.[2]

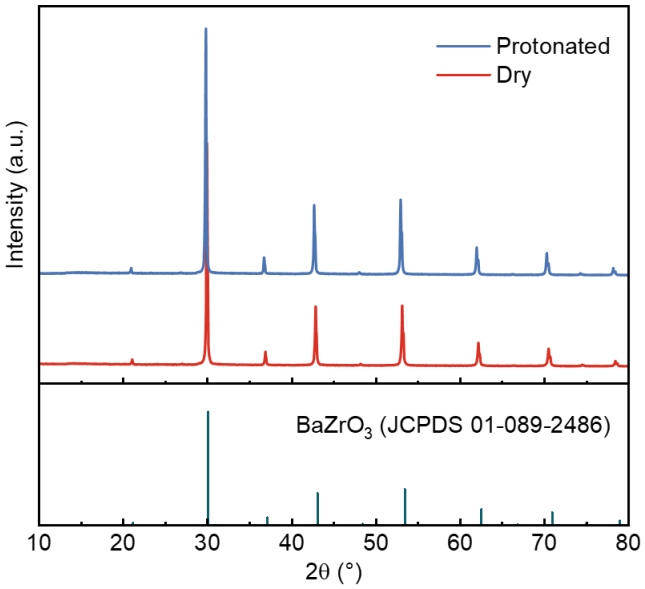

Supplementary Fig. 1. Powder XRD patterns of protonated and dry BZY.

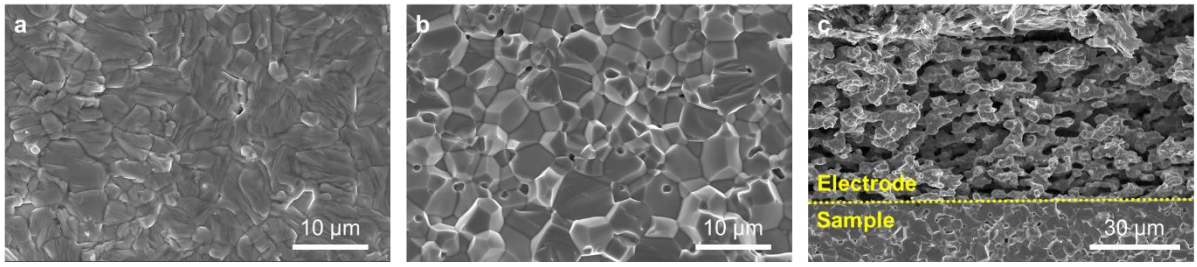

Supplementary Fig. 2. SEM images of **a** surface, **b** cross-section, and **c** electrode-sample interface of the sintered BZY pellets. The pellets are dense with a grain size range of 1−10 μm.

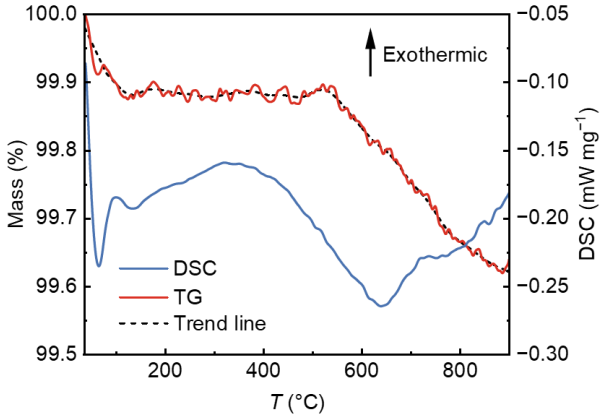

Supplementary Fig. 3. TGA and DSC curves of protonated BZY in dry N_2 from room temperature to 900 °C.

Supplementary Table 1. Proton concentration of protonated BZY measured by a Karl-Fischer moisture titrator in dry N_2 at 900 °C. The errors are the standard deviation for measurements on different samples.

Weight loss (%)	Proton concentration ($\times 10^{21}$ cm^{-3})	Proton content per unit cell	Degree of hydration (%)
0.279 ± 0.006	1.13±0.04	0.0854±0.0019	42.7±1.0

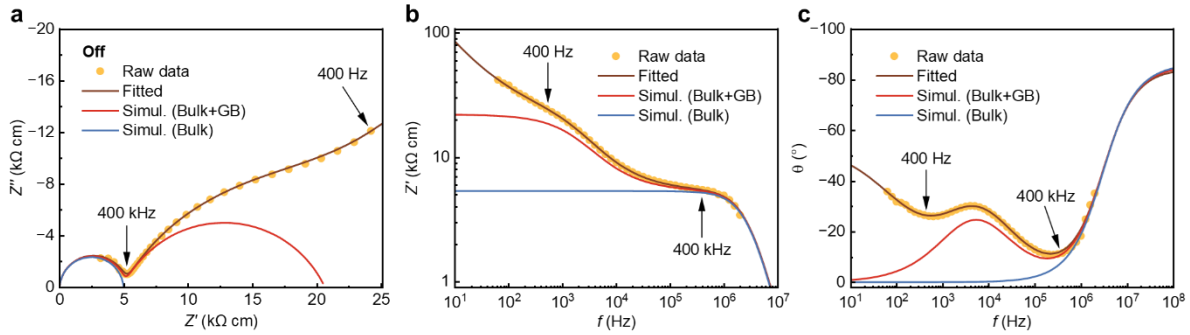

Supplementary Fig. 4. a Nyquist and **b, c** Bode plots of BZY without MIR irradiation measured at 160 °C. The fitted EIS spectrum, and the deconvoluted bulk and bulk plus GB components of proton conduction are presented. Z' at 400 kHz and 400 Hz reflect bulk and GB conduction features in the EIS spectra, respectively.

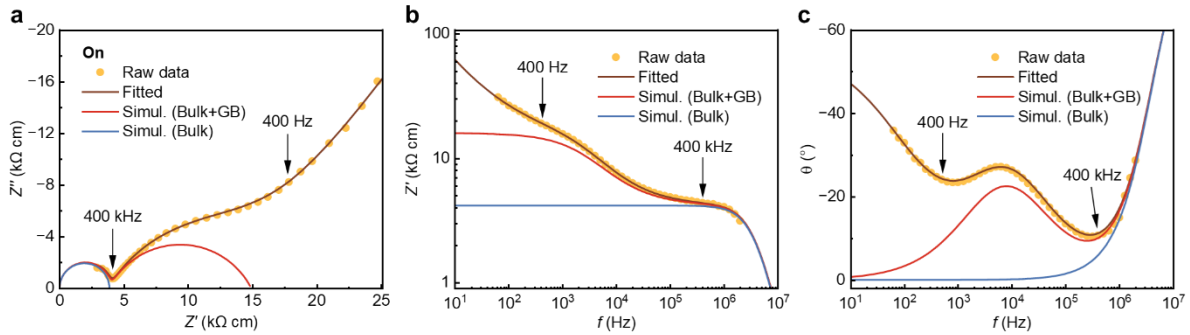

Supplementary Fig. 5. a Nyquist and **b, c** Bode plots of BZY with MIR irradiation measured at 160 °C. The fitted EIS spectrum, and the deconvoluted bulk and bulk plus GB components of proton conduction are presented. Z' at 400 kHz and 400 Hz reflect bulk and GB conduction features in the EIS spectra, respectively.

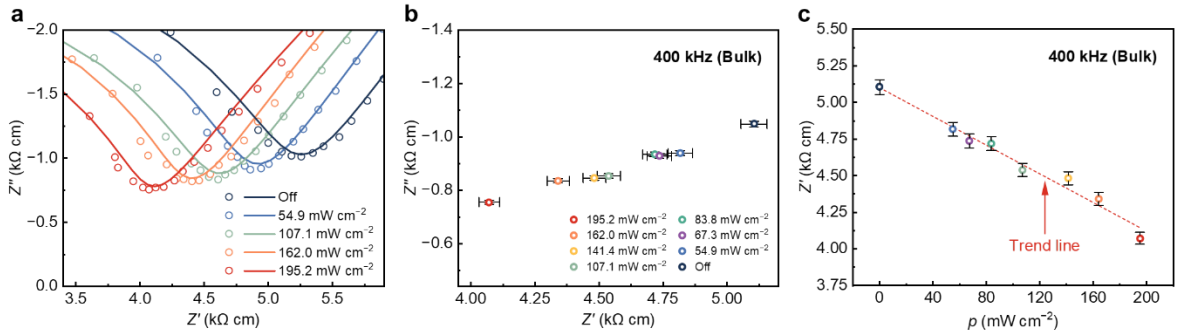

Supplementary Fig. 6. a Nyquist plots of bulk features, **b** single-point impedance and **c** Z' of BZY measured at 400 kHz and 160 °C under various effective power densities (p) of MIR

irradiation. A linearly decreasing trend of bulk proton conduction resistance with increasing power is shown in **c**.

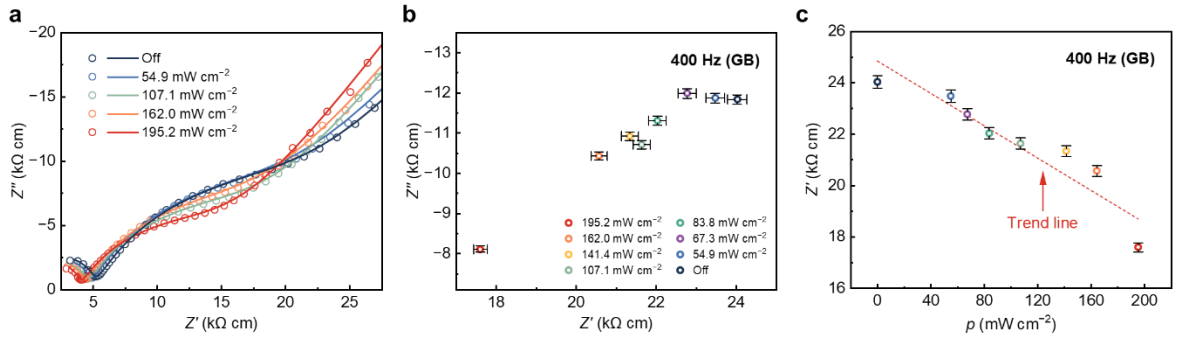

Supplementary Fig. 7. a Nyquist plots of GB features, **b** single-point impedance and **c** Z' of BZY measured at 400 Hz and 160 °C under various p of MIR irradiation. A linearly decreasing trend of GB proton conduction resistance with increasing power is shown in **c**.

Supplementary Table 2. Parameters indicating changes in proton conduction properties under different irradiation states.

Component	ΔE_a (eV)	$\sigma_0^{on}/\sigma_0^{off}$	Q^{on}/Q^{off}
Bulk	0.017±0.004	0.809±0.029	0.768±0.105
GB	~ 0	1.268±0.140	1.271±0.077

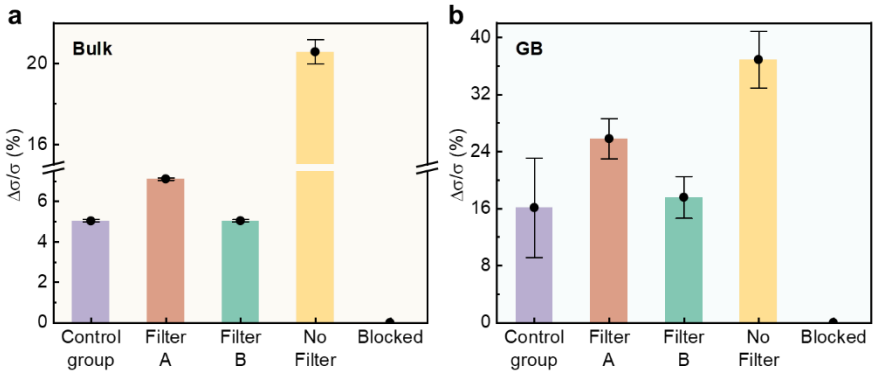

Supplementary Fig. 8. Comparison of $\Delta\sigma/\sigma$ for **a** bulk and **b** GB with and without filters and blocking. d = 1.460 mm for all cases. The MIR radiation was blocked using a 0.1 mm-thick metal plate between the sample and the light source and was not in contact with any side.

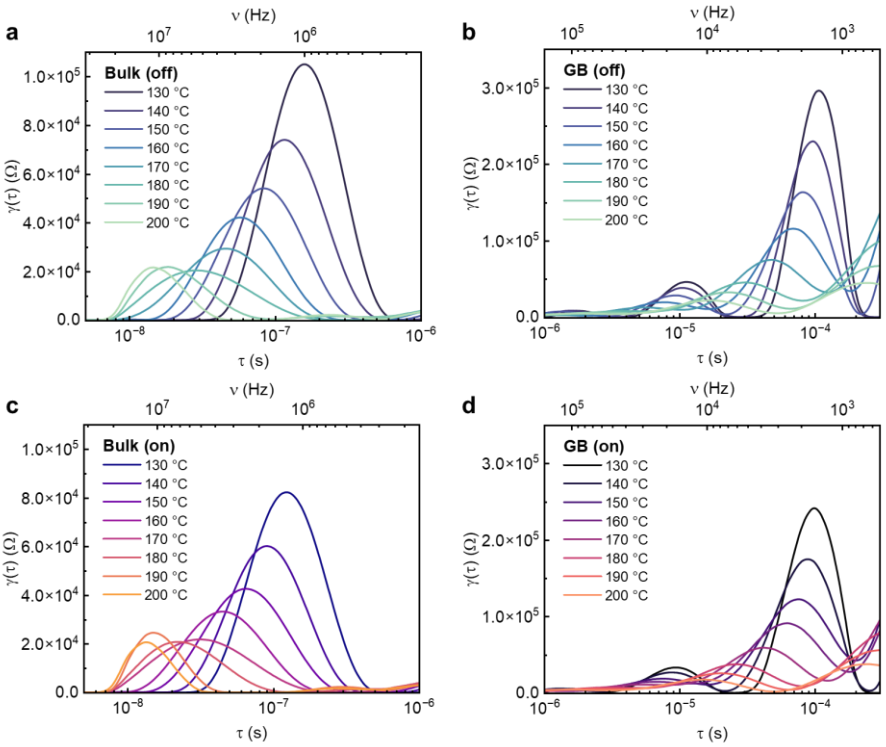

Supplementary Fig. 9. Distribution of relaxation times (DRT) curves[3] for bulk and GB **a, b** with and **c, d** without MIR irradiation obtained from the EIS spectra of the samples in 130–200 °C. Considering the inverse relation between the relaxation time and hopping frequency,[4,5] the overall trend of peak position in the DRT spectra well reflects the evolution of hopping frequency presented in Figure 3b of the main text.

Additional information about the lab-made test system

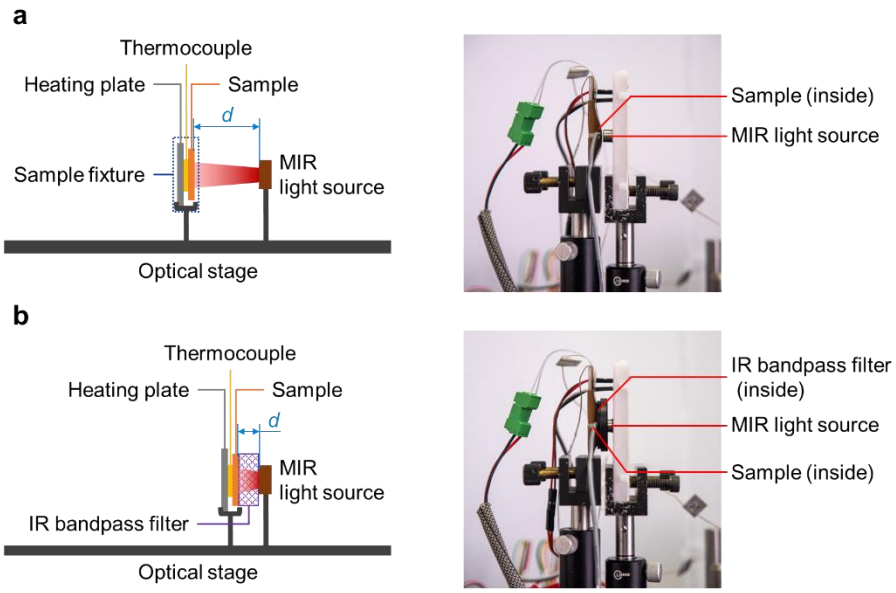

Supplementary Fig. 10. Schematic illustration and optical image for setups **a** without and **b** with the IR bandpass filter of the lab-made test system. *d* denotes the distance between top surface of the sample and emission window of the light source. The bandpass filter is in contact with sample fixture and the light source.

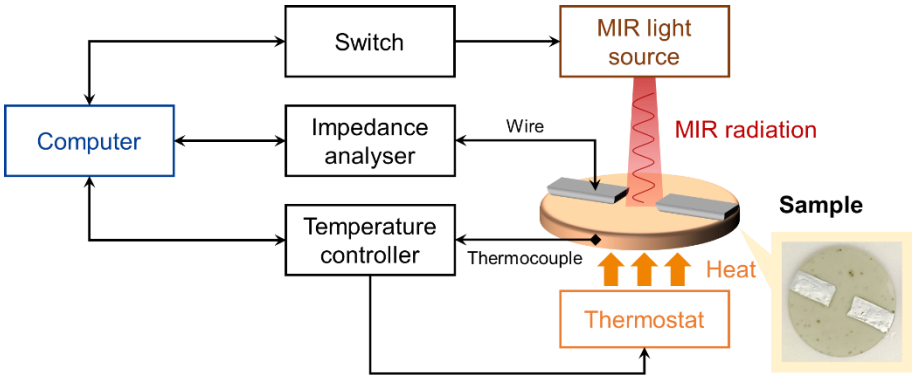

Supplementary Fig. 11. Control schematic diagram of the lab-made test system, and optical image of the BZY sample. Black arrows indicate the direction of electrical signals. The feedback loop between the heating plate, sample and temperature controller stabilizes sample temperature.

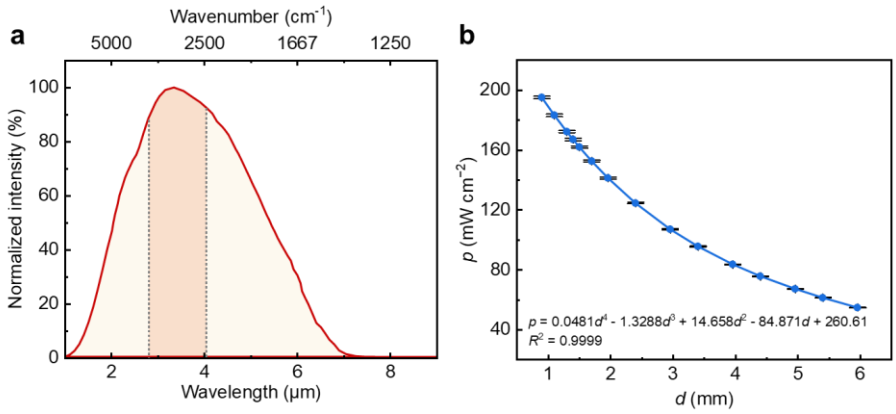

Supplementary Fig. 12. a Radiation spectrum of the MIR light source. The highlighted area (2.7−4.0 μm, orange) corresponds to the major absorption band of O–H stretching vibration and defines the wavelength for the effective power of MIR irradiation (p). **b** p as a function of d fitted to a fourth-order polynomial (R^2 = 0.9999). p was estimated from angular radiation distribution of the light source.[6]

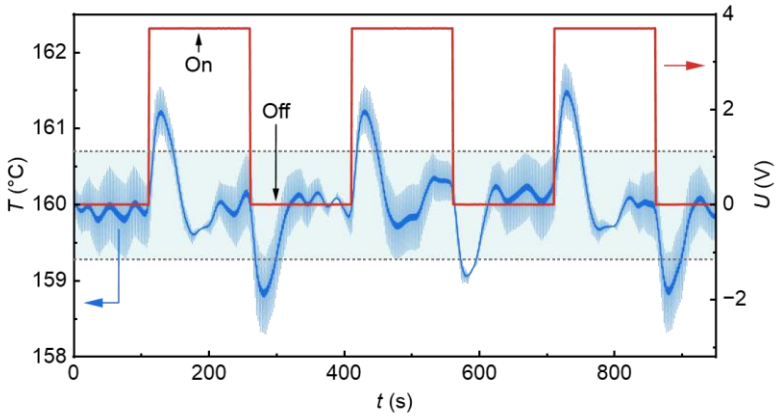

Supplementary Fig. 13. Sample temperature (T) and electrical voltage of the MIR light source (U) during several on/off cycles. Rated voltage of the light source is 3.7 V. Light blue: measured T; blue: 10 s average of T. The fluctuation of T originates from pulse width modulation of the temperature controller regulating output power of the heating plate. The set value of T is 160 °C. T is stabilized at 160±0.7 °C in approximately 100 s after the light source is turned on/off.

Supplementary Note 1: Evaluating the IR-induced heating effect on the samples

The heating effect of MIR irradiation on the samples is manifested as the percent change in conductivity ($\Delta\sigma/\sigma$) due to the temperature rise (ΔT_h) upon irradiation of light. Several parameters used to evaluate this $\Delta\sigma/\sigma$, including the specific heat capacity of the sample (C_m),

an intermediate variable $(1/\Theta)_m$ and the consequent ΔT_h, are plotted in Figures S14.

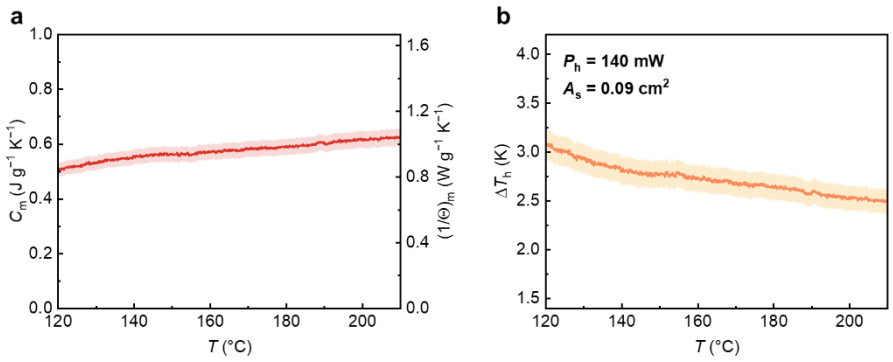

Supplementary Fig. 14. a The specific heat capacity (C_m) of the sample and the intermediate variable $(1/\Theta)_m$, and **c** the consequent ΔT_h plotted against T. Shadowed areas indicate a relative error of ±5%.

We assume that at d = 0.9 mm (the minimum of the lab-made test system), all the incident optical power (P_o = 140 mW) is concentrated to the minimum irradiated area of the sample (A_s), and is directly converted into heat flow ($P_h = P_o$).[7] ΔT_h was found in the range of 2.5–3.0 K for T in 130–200 °C. The resulting $(\Delta\sigma/\sigma)_{Bulk}$ and $(\Delta\sigma/\sigma)_{GB}$ were expected to be approximately 8% and 13%, which are lower than those observed in experiment (28.6% and 41.2%). P_h at different d was then calculated by multiplying a d-dependent coefficient, which was obtained by normalizing the function $p(d)$ (Supplementary Fig. 12b) to [0,1]. As presented in Figure 2c,d of the main text, the observed $\Delta\sigma/\sigma$ for bulk and GB due to MIR irradiation are 2–3 times greater than the estimated results due to heating. Thus, light-induced heating effect is not a major contributor to the enhancement in proton conductivity.

In the following, we explain how the above conclusion was obtained. Consider the sample as a homogeneous pellet of cross section A, thickness h and mass m. Let $\Delta T_h = T_2 - T_1$. Since h is small (< 1 mm), T_2 and T_1 were considered to represent the sample temperature with and without irradiation, and $\Delta\sigma/\sigma$ was calculated by

$$\frac{\Delta\sigma}{\sigma} = \left[\exp\left(-\frac{E_a}{k_B}\left(\frac{1}{T_2}-\frac{1}{T_1}\right)\right)-1\right]\times 100\% \quad (1)$$

Inspired by a recent study involving the light-induced heating of ultraviolet-visible radiation onto Gd-doped ceria by Defferriere et al.,[7] we supposed all the incident optical power (P_o) is

concentrated to a circular spot tangent to the irradiated area of the sample, corresponding to a cylinder slice cut parallel to the direction of incident radiation, with cross section A_s, thickness h and mass m_s (Supplementary Fig. 15). Moreover, P_o is directly converted into heat flow (P_h). The consequent ΔT_h was calculated by assuming the sample as a thermal resistor, and considering solely thermal conduction:

$$\Delta T_h = \Theta_s P_h \tag{2}$$

where Θ_s is the thermal resistance of the sample.

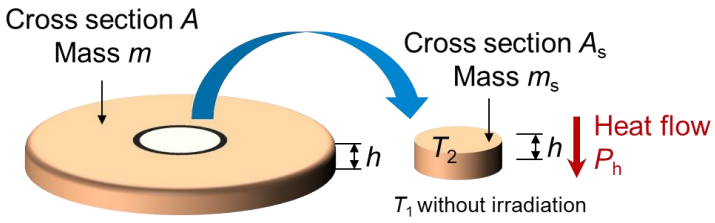

Supplementary Fig. 15. Schematic illustration of a cylinder slice from the sample with cross section A_s, thickness h and mass m_s cut parallel to the direction of incident radiation.

Through dimensional analysis, it is reasonable to evaluate Θ_s (K W^{-1}) from the specific heat capacity (C_m) of the sample, whose dimension is J g^{-1} K^{-1}. We note a similar method has been developed by Pham et al.[8] to estimate the impact of THz radiation on the temperature of solid electrolyte $Li_{0.5}La_{0.5}TiO_3$ by evaluating the inversed thermal resistance of the sample (dimension W K^{-1}). From the DSC results (heat flow signal dQ/dT) in Supplementary Fig. 3, C_m can be obtained using[9,10]

$$C_m = \frac{1}{m}\frac{dQ/dt}{dT/dt} = \frac{1}{m}\frac{\Delta Q/\Delta t}{\Delta T/\Delta t} \tag{3}$$

where m is the sample mass, and dT/dt is the heating rate. For a small sampling time interval Δt (here 0.03 min), dQ/dT and dT/dt can be approximated with $\Delta Q/\Delta t$ and $\Delta T/\Delta t$ as measured by STA, respectively. Multiplying Eq. 3 by Δt yielded an intermediate variable $(1/\Theta)_m$ (W g^{-1} K^{-1}):

$$\left(\frac{1}{\Theta}\right)_m = \frac{1}{m}\frac{dQ/dt}{dT} = \frac{1}{m}\frac{\Delta Q/\Delta t}{\Delta T} \tag{4}$$

On the other hand, by definition, $\Theta_s = h/\lambda A_s$, where λ is the thermal conductivity of the sample and is constant for a specific sample and given temperature.[11,12] Then the thermal resistances for the slice (Θ_s) and the sample (Θ) have the following relation (V and V_s denote the volumes)

$$\frac{\Theta_s}{\Theta} = \frac{A}{A_s} \propto \frac{V_s}{V} \propto \frac{m_s}{m} \quad (5)$$

providing the sample is homogeneous. Thus, Θ_s was obtained by

$$\Theta_s = \left[m_s \left(\frac{1}{\Theta}\right)_m\right]^{-1} = \frac{m}{m_s}\frac{\Delta T}{\Delta Q/\Delta t} \quad (6)$$

The parameters applied to Eq. 5 and 6 for the analysis of Θ_s are listed in Supplementary Table 3. $\Delta Q/\Delta t$ and ΔT have been included in STA results. This method for evaluating ΔT_h can be verified by Eq. 2 and $\Theta_s = h/\lambda A_s$, taking λ of $BaZrO_3$ at 400–500 K (around 4 W m^{-1} K^{-1}).[11,13] When P_h = 140 mW, the calculated ΔT_h is approximately 3.5 K, close to our results. Since the density of BZY (6.016 g cm^{-3} from XRD results) is larger than that of $BaZrO_3$ (5.96 g cm^{-3}),[14] a higher thermal conductivity λ is expected, leading to a lower ΔT_h.

Supplementary Table 3. Parameters applied to evaluate ΔT_h upon MIR irradiation in Eq. 3–6.

Measured			**Calculated**
A (cm^2)	A_s (cm^2)	m (g)	m_s (g)
1.3157±0.0003	0.0860±0.0003	1.2082±0.0005	0.0541±0.0007

Supplementary Note 2: The potential energy surface (PES) of proton hopping

As discussed in the main text, the O–H stretching vibration behaves as a highly anharmonic oscillator with a Morse potential V (Eq. 7 in the main text). The parameter α describes the curvature of the potential and was calculated to be 9.62 $Å^{-1}$ using Python code by Hill.[15] The energy gap between its ground state and the only excited state is 0.41 eV. By absorbing an MIR photon matching its vibration frequency, a small proportion of O–H bonds are brought to their excited state, significantly lowering the effective barrier for proton hopping from 0.46 eV at the ground state to only 0.05 eV. The proportion of such bonds should be positively correlated with the number of MIR photons incident to sample surface, which is proportional to p.

A more detailed PES of proton hopping can be elaborated with a symmetric, effective double-well Morse potential.[16–18] Sakurai et al. suggested a straightforward approach to express the double-well potential by placing two identical Morse potential wells in the opposite direction

with a certain separation, using[19]

$$V_{DW}(r) = V\left(r + \frac{R}{2}\right) + V\left(-r + \frac{R}{2}\right) \quad (7)$$

where R is the nearest O–O separation of protonated BZY (2.992 Å), and V is the Morse potential function. Supplementary Fig. 16 shows the calculated effective double-well potential with the saddle point as the origin of the position coordinate. The distance between two local minima of the potential (l), or the neighbouring sites for proton hopping, is measured as 0.98 Å. Such distance is sufficiently short to facilitate the random diffusion of protons on picosecond timescale ($\tau = 10^{-11}$–10^{-12} s) in the random walk model ($l^2 = 6D_r\tau$),[20] where the diffusivity D_r of BZY is on the order of 10^{-6}–10^{-4} cm^{-2} s^{-1} between 130 °C and 200 °C in previous works measured by QENS[21,22] and NMR.[1]

Supplementary Note 3: The multilayer-multiphase model for σ_{Bulk}^{on}

To elaborate the correlation between excitation of O–H stretching vibration through MIR irradiation with the enhancement in proton conductivity, we modelled the bulk conductivity under MIR irradiation (σ_{Bulk}^{on}) by developing a multilayer-multiphase model. The physical picture of proton conduction process in the bulk lattice of BZY is simpler compared with GB. The process can be illustrated based on classical hopping theory,[20] and the effective PES for proton hopping proposed in the main text and Supplementary Note S2.

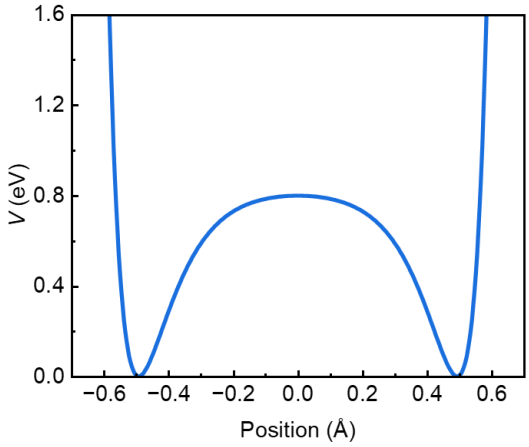

Supplementary Fig. 16. Calculated effective double-well Morse potential for the O–H stretching vibration in BZY.

To begin with, $\sigma_{\mathrm{Bulk}}^{\mathrm{on}}$ can be separated into the contributions from two parallel layers: the MIR-affected layer and the unaffected layer, with proton conductivities denoted as $\sigma_{\mathrm{Bulk}}^{\mathrm{rad}}$ and $\sigma_{\mathrm{Bulk}}^{\mathrm{off}}$, respectively (Supplementary Fig. 17a):

$$\sigma_{\mathrm{Bulk}}^{\mathrm{on}} = \frac{z}{h}\sigma_{\mathrm{Bulk}}^{\mathrm{rad}} + \frac{h-z}{h}\sigma_{\mathrm{Bulk}}^{\mathrm{off}} \tag{8}$$

where h and z are the thickness of the entire sample and the MIR-affected layer. For simplicity, ignore the interaction between MIR radiation and the sample beyond z, and let z be the characteristic penetration depth of MIR radiation in Beer-Lambert law:[7]

$$\frac{p(x)}{p_0} = \exp(-\alpha x) \tag{9}$$

where $\alpha = 1/z$ is the absorbance of MIR radiation of the sample, and has been reported to be 10.8 cm^{-1} for single-crystal $KTaO_3$.[19] Because we were unable to obtain the transmitted IR spectra of 0.9-mm thick BZY pellets, we assumed an α for the BZY pellets of 33.3 cm^{-1}, corresponding to z = 0.03 cm. The intensity distribution calculated with different α between 10.8 cm^{-1} and 100 cm^{-1} are compared in Supplementary Fig. 17b.

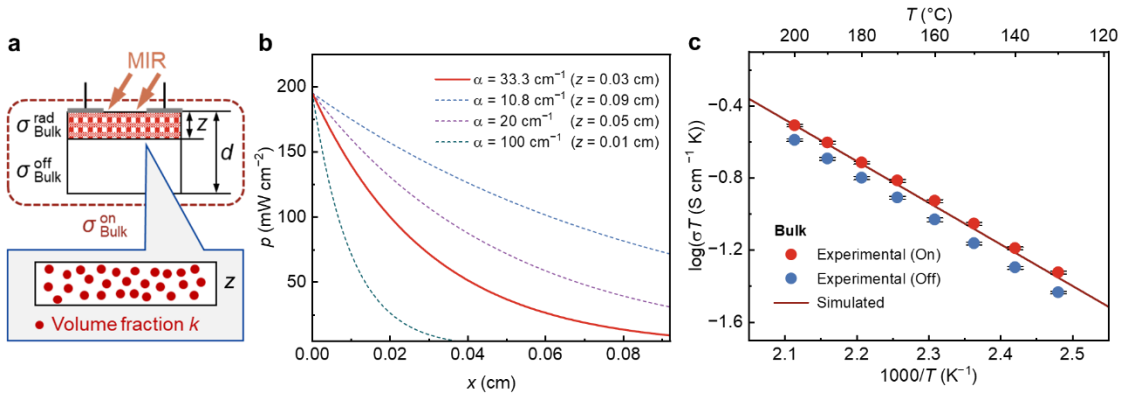

Supplementary Fig. 17. a Schematic of the multilayer-multiphase model. **b** Comparison of intensity distribution calculated with different α between 10.8 cm^{-1} and 100 cm^{-1} according to Beer-Lambert law. α = 33.3 cm^{-1} was adopted for further analysis. **c** The simulated Arrhenius plot for bulk proton conductivity (line) with MIR irradiation compared with the experimental results (scatter). Inset: Schematic of the multilayer-multiphase structure employed for the model.

To evaluate the macroscopic effect of exciting the O–H stretching vibration through MIR irradiation, $\sigma_{\mathrm{Bulk}}^{\mathrm{rad}}$ was simulated assuming MIR irradiation creates a low-E_a area in the MIR-affected layer. Therefore, the MIR-affected layer can be further modelled as a dilute dispersion

of low-E_a areas in a matrix (Supplementary Fig. 17a). In this model, the dispersed low-E_a areas have a volume fraction k, which is positively related to p and is influenced by α. Specifically, the properties of the matrix were considered equivalent to the unaffected layer (proton conductivity $\sigma^0_{Bulk} = \sigma^{off}_{Bulk}$; prefactor $\sigma^0_{0,Bulk} = \sigma^{off}_{0,Bulk}$; activation energy $E^0_{a,Bulk} = E^{off}_{a,Bulk}$).[23,24] Moreover, the dispersion of spherical low-E_a areas is assumed to exhibit high proton conductivity (σ^1_{Bulk}) due to the absorption of MIR irradiation and excitation of O–H stretching vibration in low-E_a areas. In addition, the prefactor and activation energy for σ^1_{Bulk} are denoted as $\sigma^1_{0,Bulk}$ and $E^1_{a,Bulk}$. Such consideration enables the application of Maxwell-Wagner model to analyse σ^{rad}_{Bulk}:[23,24]

$$\sigma^{rad}_{Bulk} = \sigma^0_{Bulk}\frac{2\sigma^0_{Bulk}+\sigma^1_{Bulk}+2k\left(\sigma^1_{Bulk}-\sigma^0_{Bulk}\right)}{2\sigma^0_{Bulk}+\sigma^1_{Bulk}-k\left(\sigma^1_{Bulk}-\sigma^0_{Bulk}\right)} = \sigma^0_{Bulk}\frac{2(1-k)+(1+2k)\frac{\sigma^1_{Bulk}}{\sigma^0_{Bulk}}}{(2-k)+(1-k)\frac{\sigma^1_{Bulk}}{\sigma^0_{Bulk}}} \quad (10)$$

Combining Eq. 8 and 10, and applying the Arrhenius relation of proton conductivity, σ^{on}_{Bulk} is eventually given by

$$\begin{aligned}\sigma^{on}_{Bulk} &= \sigma^{off}_{Bulk}\left[\frac{z-d}{d}+\frac{z}{d}\frac{2(1-k)+(1+2k)\frac{\sigma^1_{Bulk}}{\sigma^0_{Bulk}}}{(2-k)+(1-k)\frac{\sigma^1_{Bulk}}{\sigma^0_{Bulk}}}\right] \\ &= \sigma^0_{0,Bulk}\exp\left(-\frac{E^0_{a,Bulk}}{k_BT}\right)\left[\frac{z-d}{d}+\frac{z}{d}\frac{2(1-k)+(1+2k)\frac{\sigma^1_{0,Bulk}}{\sigma^0_{0,Bulk}}\exp\left(-\frac{E^1_{a,Bulk}-E^0_{a,Bulk}}{k_BT}\right)}{(2-k)+(1-k)\frac{\sigma^1_{0,Bulk}}{\sigma^0_{0,Bulk}}\exp\left(-\frac{E^1_{a,Bulk}-E^0_{a,Bulk}}{k_BT}\right)}\right]\end{aligned} \quad (11)$$

Supplementary Fig. 17c indicates that the simulated temperature-dependent σ^{on}_{Bulk} is in good agreement with the experimental values. The simulated results slightly smaller since we simply employed a rigid boundary for the MIR-affected layer, and the contribution from lattice and O–H wag vibrations are not taken into account in our model.[16,18,19] Additionally, by substituting into Eq. 8 with the simulated value of σ^{on}_{Bulk} using Eq. 11, experimental σ^{off}_{Bulk} at 160 °C, along with the values in Supplementary Table 4, σ^{rad}_{Bulk} can be solved, and the corresponding the enhancement in proton conductivity of the MIR-affected layer $(\Delta\sigma/\sigma)^{rad}_{Bulk}$ is in 90–105% when the volume fraction of the dispersed low-E_a region is 16.6 ± 0.7% upon MIR excitation. In summary, despite the simple shape of PES, the bulk proton conductivity obtained by our multilayer-multiphase model based on partial excitation of O–H stretching vibration in the samples is close to the experimental results.

Supplementary Table 4. Parameters for evaluating $\sigma_{\mathrm{Bulk}}^{\mathrm{on}}$ in Eq. 11.

Parameter	Value	Remarks
Prefactor without irradiation $\sigma_{0,\mathrm{Bulk}}^{0}$ (S cm^{-1} K)	2×10^4	Fitted result of Figure 3a
Prefactor with irradiation $\sigma_{0,\mathrm{Bulk}}^{1}$ (S cm^{-1} K)	1×10^4	Estimated to the same order of magnitude as $\sigma_{0,\mathrm{Bulk}}^{0}$
Activation energy without irradiation $E_{\mathrm{a,Bulk}}^{0}$ (eV)	0.459	Fitted result of Figure 3a
Activation energy with irradiation $E_{\mathrm{a,Bulk}}^{1}$ (eV)	0.050	Estimated result of Figure 4c
Sample thickness d (cm)	0.092	Measured result
MIR-affected layer thickness z (cm)	0.030	Assumed result
Volume fraction of low-E_{a} areas k	0.166±0.007	Least-square fitted result of Eq. 11

References

1. Yamazaki, Y. *et al.* Proton trapping in yttrium-doped barium zirconate. *Nat. Mater.* **12**, 647–651 (2013).
2. Han, D., Okumura, Y., Nose, Y. & Uda, T. Synthesis of $La_{1-x}Sr_xSc_{1-y}Fe_yO_{3-\delta}$ (LSSF) and measurement of water content in LSSF, LSCF and LSC hydrated in wet artificial air at 300°C. *Solid State Ionics* **181**, 1601–1606 (2010).
3. Wan, T. H., Saccoccio, M., Chen, C. & Ciucci, F. Influence of the Discretization Methods on the Distribution of Relaxation Times Deconvolution: Implementing Radial Basis Functions with DRTtools. *Electrochimica Acta* **184**, 483–499 (2015).
4. Lyagaeva, J. G., Vdovin, G. K. & Medvedev, D. A. Distinguishing Bulk and Grain Boundary Transport of a Proton-Conducting Electrolyte by Combining Equivalent Circuit Scheme and Distribution of Relaxation Times Analyses. *J. Phys. Chem. C* **123**, 21993–

21997 (2019).

5. Kuzmin, A. V., Plekhanov, M. S. & Lesnichyova, A. S. Influence of impurities on the bulk and grain-boundary conductivity of $CaZrO_3$-based proton-conducting electrolyte: A distribution of relaxation time study. *Electrochimica Acta* **348**, 136327 (2020).
6. INFRASOLID - Thermal infrared emitters. https://www.infrasolid.com/en/product/black-body-infrared-emitters-his550r-0 (2024).
7. Defferriere, T., Klotz, D., Gonzalez-Rosillo, J. C., Rupp, J. L. M. & Tuller, H. L. Photo-enhanced ionic conductivity across grain boundaries in polycrystalline ceramics. *Nat. Mater.* **21**, 438–444 (2022).
8. Pham, K. H. *et al.* Correlated Terahertz phonon-ion interactions dominate ion conduction in solid electrolyte $Li_{0.5}La_{0.5}TiO_3$. Preprint at http://arxiv.org/abs/2305.01632 (2024).
9. Guo, Y. *et al.* Structural Relaxation of Polymer Nanospheres under Soft and Hard Confinement: Isobaric *versus* Isochoric Conditions. *ACS Nano* **5**, 5365–5373 (2011).
10. Huo, M., Ma, M., Teng, Y., Xiao, Y. & Guo, Y. Suppressed physical aging in PMMA-titanium oxide nanocomposites by controlling alignment of nanoparticles. *J. Appl. Polym. Sci.* **140**, e54030 (2023).
11. Liu, Y. *et al.* Theoretical and experimental investigations on high temperature mechanical and thermal properties of $BaZrO_3$. *Ceram. Int.* **44**, 16475–16482 (2018).
12. Qiao, Z., Li, S., Li, Y., Xu, N. & Xiang, K. Structure, mechanical properties, and thermal conductivity of $BaZrO_3$ doped at the A-B site. *Ceram. Int.* **48**, 12529–12536 (2022).
13. Vassen, R., Cao, X., Tietz, F., Basu, D. & Stöver, D. Zirconates as New Materials for Thermal Barrier Coatings. *J. Am. Ceram. Soc.* **83**, 2023–2028 (2000).
14. Persson, K. Materials Data on $BaZrO_3$ (SG:221) by Materials Project. (2014) doi:10.17188/1207509.
15. Hill, C. *Learning Scientific Programming with Python*. (Cambridge University Press, New York, 2020).
16. Spahr, E. J. *et al.* Giant enhancement of hydrogen transport in rutile TiO_2 at low temperatures. *Phys. Rev. Lett.* **104**, 205901 (2010).
17. Coduri, M., Karlsson, M. & Malavasi, L. Structure–property correlation in oxide-ion and proton conductors for clean energy applications: recent experimental and computational

advancements. *J. Mater. Chem. A* **10**, 5082–5110 (2022).

18. Spahr, E. J. *et al.* Proton tunneling: a decay channel of the O-H stretch mode in $KTaO_3$. *Phys. Rev. Lett.* **102**, 075506 (2009).
19. Sakurai, A., Ando, K. & Ashihara, S. Ultrafast proton/deuteron dynamics in $KTaO_3$ observed with infrared pump-probe spectroscopy: Toward understanding of proton conduction mechanism in solid oxides. *J. Chem. Phys.* **149**, 104502 (2018).
20. Gao, Y. *et al.* Classical and emerging characterization techniques for investigation of ion transport mechanisms in crystalline fast ionic conductors. *Chem. Rev.* **120**, 5954–6008 (2020).
21. Braun, A. *et al.* Proton diffusivity in the $BaZr_{0.9}Y_{0.1}O_{3-\delta}$ proton conductor. *J. Appl. Electrochem.* **39**, 471–475 (2009).
22. Braun, A. & Chen, Q. Experimental neutron scattering evidence for proton polaron in hydrated metal oxide proton conductors. *Nat. Commun.* **8**, 15830 (2017).
23. De Lima, O. A. L. & Sharma, M. M. A generalized Maxwell-Wagner theory for membrane polarization in shaly sands. *GEOPHYSICS* **57**, 431–440 (1992).
24. Bonanos, N. *et al.* Applications of Impedance Spectroscopy. in *Impedance Spectroscopy* (eds. Barsoukov, E. & Macdonald, J. R.) 175–478 (Wiley, 2018). doi:10.1002/9781119381860.ch4.